Journal of Energy Storage 73 (2023) 109235

Contents lists available at ScienceDirect

Journal of Energy Storage

journal homepage: www.elsevier.com/locate/est

Research Papers

A CFD results-based reduced-order model for latent heat thermal energy storage systems with macro-encapsulated PCM

Andreas König-Haagen [a], Moritz Faden [b], Gonzalo Diarce [a,*]

[a] ENEDI Research Group, Department of Energy Engineering, Faculty of Engineering of Bilbao, University of the Basque Country UPV/EHU, Bilbao, Spain
[b] Chair of Engineering Thermodynamics and Transport Processes (LTTT), Center of Energy Technology (ZET), University of Bayreuth, Bayreuth, Germany

ARTICLE INFO

Keywords:
Computational fluid dynamics (CFD)
System simulation
Latent heat thermal energy storage system
Macro-encapsulated
PCM

ABSTRACT

Macro-encapsulation of phase change material (PCM) is a promising approach to overcome a serious drawback of many latent heat thermal energy storage systems (LHTESSs): their low thermal power. Simulations are often used to support the design of these storage systems, but the simulation of the charging process of such an LHTESS with detailed CFD models is too computationally expensive. To obtain information about the behavior of a complete LHTESS, highly simplified system simulation models are usually applied. A new approach to create a reduced-order model is herein presented that aims to increase the accuracy of these system simulation models. The first step consists of performing a set of detailed CFD simulations of one capsule with different boundary conditions. The results are written into look-up tables that contain the charging power of one capsule as a function of the enthalpy stored and the boundary conditions. These look-up tables are then implemented into the reduced-order model. The temporal mean deviation of the energy content in the storage unit between experiments and the reduced-order model is only 5 % and the simulation time of the fastest reduced-order model was 5 s, while the CFD simulations took up to about two weeks on a workstation. Finally, for the conditions tested, the heat transfer fluid (HTF) does not have to be included in the CFD simulation, but can be replaced by a properly defined convective boundary condition. The capsule wall, however, needs to be included in the CFD model (especially for capsule wall materials with a distinctively higher thermal conductivity than the PCM) to account for the heat flow towards the bottom of the capsule supporting close contact melting.

1. Introduction

Storing energy efficiently and cost-effectively is one of the greatest challenges of our time. Latent heat thermal energy storage systems (LHTESSs) store thermal energy based on a solid/liquid phase change of a phase change material (PCM) and play a key role when it comes to storing thermal energy in a dense way [1]. The macro-encapsulation of PCMs is a promising approach to overcome a severe drawback of many PCMs, which is their low thermal conductivity [2]. This low thermal conductivity generally leads to low discharging (solidification) powers of the LHTESS. Macro-encapsulation overcomes this disadvantage through an increased heat transfer area between the heat transfer fluid (HTF) and the PCM (usually separated by a heat exchanger), since the PCM is no longer placed as bulk in the LHTESS but in a large number of capsules [2]. In many cases, not only the discharging but also the charging (melting) power is thereby increased due to the larger heat transfer area and close contact melting (CCM). CCM occurs, for instance, when an unfixed PCM with a denser solid than liquid phase melts in a capsule, leading to a sinking of the solid PCM which forms a thin melting gap at the bottom of the capsule.

Designing LHTESSs is a difficult task that often includes time-consuming experiments and numerical simulations. Moreover, to study the behavior of an LHTESS in its application, one has to include a realistic representation of the system containing the LHTESS. In addition, a lot of different boundary conditions have to be tested, which is often not feasible for experiments or detailed simulations. With simplified simulation, it is possible for models to perform parameter variations; however, these models have limited accuracy, especially for complex physical phenomena such as CCM.

Detailed simulations of LHTESSs are generally performed with computational fluid dynamics (CFD). Many approaches have been developed to describe the solidification and melting process – not only for LHTESSs, but for many different applications [3–5]. So far the enthalpy porosity method [6] is the most commonly applied method to

* Corresponding author.
E-mail address: gonzalo.diarce@ehu.es (G. Diarce).

https://doi.org/10.1016/j.est.2023.109235
Received 21 May 2023; Received in revised form 24 August 2023; Accepted 6 October 2023
Available online 17 October 2023

account for the solid/liquid phase change, which includes describing the solid and liquid phase as one phase. The velocity in the solid is suppressed with a Darcy term and the phase change enthalpy is included in the energy equation employing a source term. It has been demonstrated several times [3,7,8] that, within the family of enthalpy methods, the so-called optimum approach [7] has advantages over the other approaches in terms of calculation speed and accuracy. Unfortunately, the enthalpy porosity method cannot be directly used to model CCM (which includes the settling of the solid PCM), since it suppresses the movement of the solid PCM. An approach that just integrates a smaller Darcy constant to lessen the effect of the Darcy term has often been tried, but is doomed to fail since it does not represent the increased melting rate by CCM, but by a lower resistance of the solid to convection. Thus, even if melting rates similar to those of the experiment can be observed in one case by tuning the Darcy constant, no reliable conclusions can be made for other conditions.

Over the years, many physically reasonable approaches have been developed to account for CCM in numerical simulations. One of the first was presented by Asako et al. [9] and methods based on a variable viscosity method [10,11] and Euler-Lagrange methods [12,13] were developed later – a comprehensive overview can be found in literature [14]. The method used in the present paper is based on the enthalpy porosity approach, but instead of forcing the solid velocity to zero, the Darcy term is used to impose a settling velocity calculated from a force balance on the solid PCM [15,16]. To date, most numerical models of macro-encapsulated PCM do not include the HTF or the capsule wall and they rarely pay special attention to boundary conditions. However, simulations of CCM with detailed boundary conditions [17], or even models including the capsule and a surrounding HTF, have recently been presented [18,19]. Unfortunately, as these simulations are very time-consuming, running a detailed CFD simulation of a complete LHTESS with macro-encapsulated PCM is not operative with today's computers.

For complete LHTESSs, simplified system simulation models are used. Normally these models describe the capsules and the HTF as separate phases [20,21]. An interesting approach to increase the accuracy of the system simulation models is to determine the effective thermal conductivity of the PCM with CFD simulations. This was done, for instance, for a finned shell-and-tube LHTESS [22,23]. For LHTESSs with macro-encapsulated PCMs, CFD results of CCM were used to fit a correlation implemented in a local thermal non-equilibrium CFD model of the overall storage [24]. A limiting aspect of this model is the fact that the Rayleigh number is used in the correlations, which originally describes natural convection and not CCM. An alternative approach was developed recently which incorporates CFD results of CCM into system simulation models of LHTESSs with macro-encapsulated PCMs with the help of look-up tables [25]. While this approach seems promising, some open questions remain, such as whether or not the capsule wall and the HTF have to be included in the CFD models. Therefore, based on the shortcomings in the literature, the objectives of the present paper are the following:

- Build a CFD model for a PCM-filled macro-capsule with surrounding HTF in three different levels of detail: i) only PCM; ii) PCM, the air above the PCM and the capsule wall; iii) PCM, the air above the PCM, the capsule wall and the HTF.
- Assess whether the capsule wall and the HTF have to be included in the CFD model or if they can be substituted by appropriate boundary conditions.
- Build a simplified model of a complete LHTESS that uses the results of a parameter variation for single capsules performed with the CFD models.
- Compare the results of the simplified model to experimental results.
- Analyze the accuracy of the simplified model and compare its uncertainty to that reported in the literature for CFD simulations of similar LHTESSs.

To address these points, the paper is structured as follows: After the introduction, the experiments are described in Section 2. The numerical models are derived in Section 3 and their mesh independency is presented in Section 4. The results are presented in Section 5 and discussed in Section 6.

2. Experiments

The experiments were conducted for comparison with the numerical results. The experimental setup and the boundary and initial conditions are described in this section.

2.1. Experimental setup

The experimental setup consists of an LHTESS with cylindrical alumina macro-capsules filled with octadecane. A flow chart of the LHTESS is shown in Fig. 12 in Appendix A and a detailed description of this LHTESS can be found elsewhere [26]. The capsules are standing and are stacked in two levels of 16 capsules each. The height of the capsules is 0.25 m, the diameter is 0.06 m and the wall thickness is 3 mm. The storage container is made of stainless steel and insulated with 100 mm thick mineral wool panels. Perforated plates are installed at the top and bottom to guarantee a uniform flow of the water used as HTF. Resistance thermometers are located at the inlet and outlet of the LHTESS so that the HFT temperature at those points is monitored. Furthermore, the mass flow of the water is measured at the inlet. The masses and heat capacities of the different parts of the LHTESS [26] are shown alongside the material properties of the PCM [27] in Table 1.

2.2. Boundary and initial conditions

For comparison with the numerical model, a melting experiment was performed three times (*experiment 1, experiment 2* and *experiment 3*) with the above-described LHTESS. For the experiments, the LHTESS was initially at a uniform temperature of 20 °C. The inlet temperature of the HTF was about 35°C and the mass flow of the HTF was 6.6 kg/min. Both the inlet temperature and the mass flow varied over time. The HTF entered from the top of the LHTESS.

3. Numerical models

Two different types of models were applied: i) CFD models for detailed simulations of a single capsule or a single capsule with surrounding HTF; and ii) reduced-order models that use the results of the CFD models to predict the behavior of a complete storage unit

Table 1
Masses and heat capacities of the PCM, the HTF and the storage parts [26,27].

Name	Material	Property	Value	Unit
PCM	Octadecane	m	12.32	kg
		c_s	1.91	kJ/(kg • K)
		c_l	2.24	kJ/(kg • K)
		L	237	kJ/kg
		T_s	301.125	K
		T_l	301.135	K
		ρ	777	kg/m^3
		β	$8.68 \bullet 10^{-4}$	1/K
		η	$3.54 \bullet 10^{-3}$	Pa • s
		λ_s	0.334	W/(m • K)
		λ_l	0.151	W/(m • K)
Capsules	Alumina	m	14.45	kg
		c	0.89	kJ/(kg • K)
Perforated plates	Alumina	m	7.5	Kg
		c	0.89	kJ/(kg • K)
Storage tank etc.	Stainless steel	m	35.29	kg
		c	0.5	kJ/(kg • K)
HTF	Water	m	16.80	kg

containing many capsules. The simulation approach is depicted in Fig. 1, while Fig. 2 shows the part of the LHTESS that was simulated with the reduced-order models (left) and the CFD models (right).

In the first step (depicted as "1. Creation of the look-up table" in Fig. 1) the $\dot{Q}$ values from the CFD models were written to a look-up table depending on three or two dimensions representing the HTF temperature, the mass flow or a heat transfer coefficient and the total energy in the cell. For a constant heat transfer coefficient, the look-up table has two instead of three dimensions. Applying the look-up table within a reduced-order model is schematically shown as "2. Applying the reduced-order model" in Fig. 1.

This approach neglects heat conduction between different height-levels and assumes that capsules in one level will behave identically, that there is no significant back-flow of the HTF and that a single value of the total energy in one capsule, or one capsule with surrounding HTF, is sufficient to predict its heat transfer behavior. The last point implies that the enthalpy distribution within the capsule, or the capsule with surrounding HTF, is not explicitly needed to predict heat transfer. This assumption was checked in previous work for a similar case and was valid for a broad range of parameters, as long as the capsule is charged monotonously and not discharged in between [25].

Three different CFD models were developed, which differ in that the HTF, the capsule wall and the air above the PCM are considered in the CFD model or not. The corresponding reduced-order models for system simulations were adjusted accordingly. An overview of the models developed can be found in Table 2. Their details are provided next.

3.1. CFD models

For all of the 3 models developed, it was assumed that the cylindrical simulation domain can be represented in 2D using the middle axis of the cylinder as a symmetry line. All CFD models were implemented in OpenFOAM [28] (ESI OpenCFD Release OpenFOAM® v1812) with a mesh of 60,000 cells in the PCM region that was strongly refined towards the bottom of the capsule – the melt gap is thinner than 1 mm and must be sufficiently resolved to cover the fluid flow of the melted PCM. The *CFD-PCM* model is based on a previously validated model [15] and is also the core of the other two CFD models. Therefore, in the upcoming paragraphs, the *CFD-PCM* model is described first, followed by the other two models.

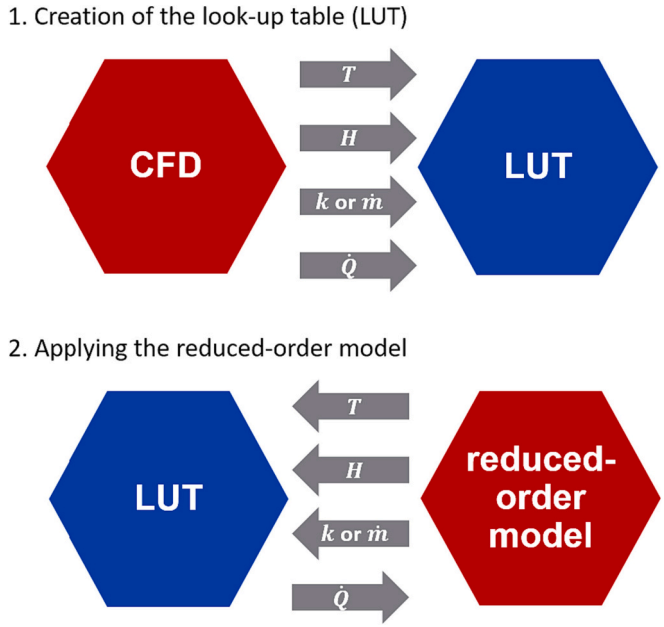

Fig. 1. Schematic representation of the overall simulation approach.

3.1.1. CFD-PCM

The energy conservation for the PCM is Eq. (1):

$$\frac{\partial h}{\partial t} + \nabla \bullet (\vec{u} h) = \nabla \bullet \left(\frac{\lambda}{\rho} \nabla T \right) \tag{1}$$

Here, it is important to note that all the enthalpy h is transported in the convective term and not only the sensible part. This is necessary to allow the solid PCM to settle. Unlike in Faden et al. [15], Eq. (1) is not solved with the classical source-based method [29] but with the source-based variant of the optimum approach [30], which speeds up the simulation significantly.

The model assumes a constant density in the continuity equation (Eq. (2)), therefore it reads as follows:

$$\nabla \bullet \vec{u} = 0 \tag{2}$$

The assumption of a constant density can lead to large errors in the simulation of solid/liquid phase change problems [31]. However, by taking the liquid density and the correct mass of the PCM, this error can be minimized since the height of the PCM in contact with the wall at the beginning of the melting process equals the filling height with completely liquid PCM (as long as the density of the liquid PCM is smaller than the density of the solid PCM). The momentum equation for the PCM is (Eq. (3)):

$$\frac{\partial \vec{u}}{\partial t} + \nabla \bullet (\vec{u}\vec{u}) = -\nabla \frac{p}{\rho} + \nabla \bullet (\nu \nabla \vec{u}) + \left(1 - \beta\left(T - T_{ref}\right)\right) \vec{g} + \vec{A} \tag{3}$$

with the Darcy term (Eq. (4))

$$\vec{A} = \frac{D}{\rho} \frac{(1-\alpha)^2}{\alpha^3 + \epsilon} \left(\vec{u} - \vec{u}_{set} \right) \tag{4}$$

where the large Darcy constant D was set to 10^{10} and the small Darcy constant ϵ set to 10^{-3}. The calculation of the settling velocity $\vec{u}_{set}$ is performed via a force balance. The forces acting on the solid PCM body are (Eq. (5)):

$$\vec{F} = \underbrace{-\oint_s p \bullet d\vec{S}}_{\vec{P}} + \underbrace{\oint_s \tau \bullet d\vec{S}}_{\vec{D}} + \underbrace{\int_V \rho_s \vec{g} dV}_{\vec{G}} \tag{5}$$

With the pressure force $\vec{P}$, the viscous force $\vec{D}$ and the weight force $\vec{G}$. As $\vec{F} = \vec{a} \bullet m$, Eq. (5) renders:

$$\underbrace{\int_V \rho_s dV \, d\frac{\vec{u}_{set}}{dt}}_{\vec{I}} = \vec{P} + \vec{D} + \vec{G} \tag{6}$$

Next, Eq. (6) is interpreted as a function of $\vec{u}_{set}$, as originally proposed by Asako et al. [9] and $\vec{D}$ and $\vec{I}$ are neglected, as they are several orders of magnitude smaller than $\vec{P}$ and $\vec{G}$ – resulting in Eq. (7).

$$f\left(\vec{u}_{set}\right) = \vec{P} + \vec{G} = 0 \tag{7}$$

The momentum equation was solved with the PISO algorithm [32] and the settling velocity was calculated implicitly [15]. In contrast to our previous publication [15], the calculation of the surface of the solid body is now – inspired by the work of Hummel et al. [18] – done by the isoSurface function/algorithm implemented in OpenFOAM.

On the top, the bottom and the side wall, a Cauchy boundary condition is imposed accounting for the convective heat transfer of the HTF and the heat transfer resistance of the capsule wall. Two different correlations were implemented, one for a plane wall and one for a concentric annular gap [33]. These are indicated as "*var*" and "*fix*", respectively.

3.1.2. CFD-PCM-air-wall

In addition to the PCM, this model includes the air and the capsule

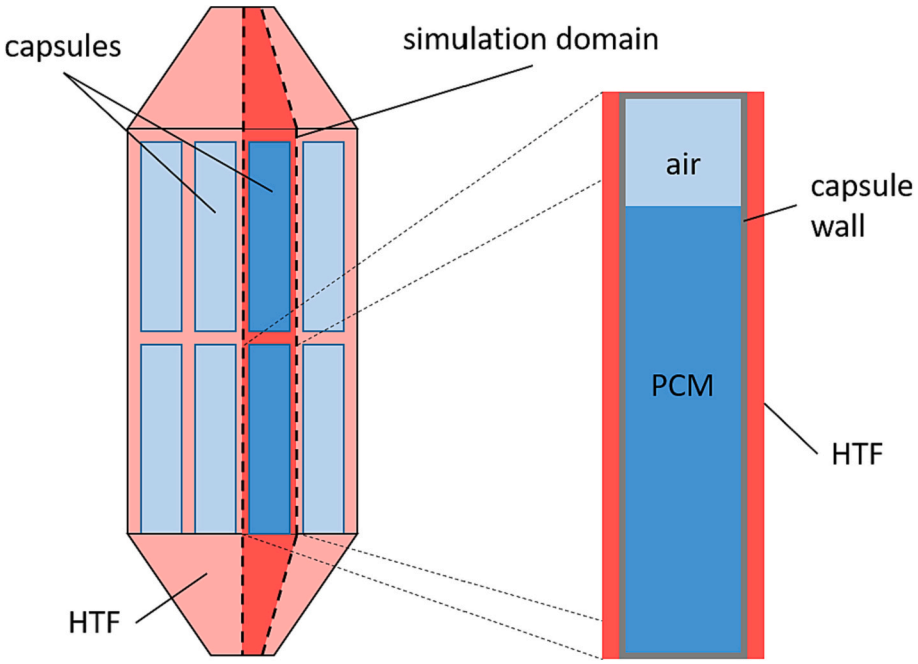

Fig. 2. Schematic view of the simulation domain.

Table 2
Overview of the numerical models involved in this study.

CFD model	Reduced-order models for system simulations	Variations	PCM	Air	Capsule wall	HTF	Storage container etc.
CFD-PCM	*sys-CFD-PCM*	*-var/-fix*	CFD	X	sys	sys	sys
CFD-PCM-air-wall	*sys-CFD-PCM-air-wall*	*-var/-fix*	CFD	CFD	CFD	sys	sys
CFD-PCM-air-wall-HTF	*sys-CFD-PCM-air-wall-HTF*	X	CFD	CFD	CFD	CFD	sys

wall. In the air, only heat conduction is considered. This was done since the simulation time would increase drastically by including the natural convection of the air and, more importantly, the effect of the air on the heat transfer process is negligible – it mainly acts as insulation. A convective boundary condition accounting for the HTF was used on the side wall. The top and the bottom walls were assumed to be adiabatic due to the small temperature gradient along the fluid flow of the HTF, which results in small temperature changes from one level of capsules to the next.

3.1.3. *CFD-PCM-air-wall-HTF*

This model is identical to the *CFD-PCM-air-wall* model, except for the HTF, which is included in the simulation domain here. It was assumed that the cell containing the capsule and the HTF can be represented by a cylindrical shape with the same volume as the actual geometry. The inlet velocity and temperature of the HTF were given as boundary conditions and a zero gradient condition was imposed on the outer side of the HTF domain.

3.2. *Reduced-order models*

All reduced-order models were implemented in MATLAB® R2021b and represent the storage as a one-dimensional stack of layers of capsules surrounded by the HTF (see Fig. 2). It is assumed that all capsules within a layer behave identically. Each cell (containing one capsule and the corresponding HTF) is represented by one node of the model. On top of and below these nodes there is another node representing the HTF within the inlet and outlet. A schematic view of the discretization can be seen in Fig. 3.

The thermal mass of the storage tank and other components (e.g. perforated plates) is distributed proportionally among the nodes. The

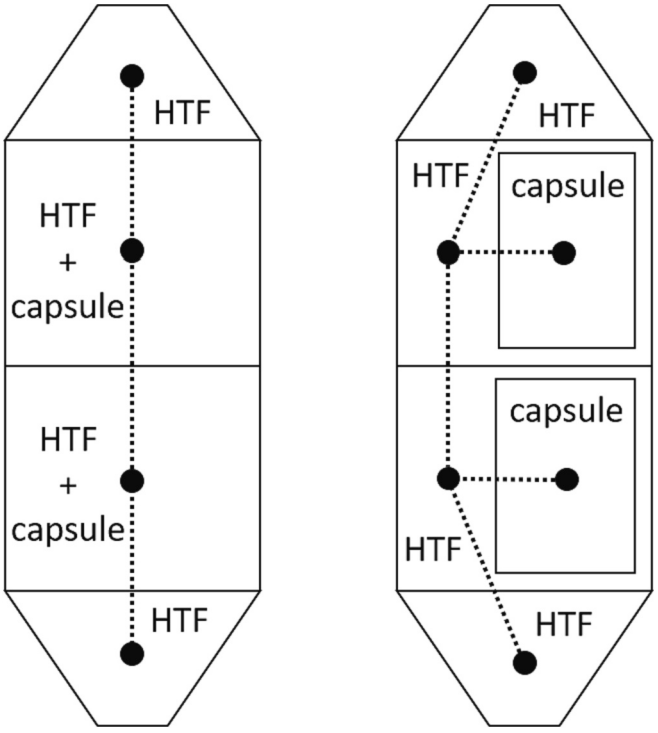

Fig. 3. Schematic view of the discretization of the reduced-order models (left: sys-CFD-PCM-air-wall-HTF, right: sys-CFD-PCM and sys-CFD-PCM-air-wall).

heat loss coefficient of the LHTESS was estimated with the help of steady-state experiments and is $R_{loss} = 0.389$ K/W for the overall storage. Since a constant density is assumed for the HTF, Eq. (2) also holds for the reduced-order models and, in consequence, the incoming mass flow equals the outcoming mass flow in each cell. By neglecting friction and pressure losses, it is sufficient to solve only the energy equation for these 1D models. The heat transfer in and out of the cells and the capsules is modeled depending on the type of system simulation model and is described below.

3.2.1. sys-CFD-PCM

The energy equation for the *sys-CFD-PCM* model is for cells containing a PCM capsule (Eq. (8))

$$\frac{\partial H^*}{\partial t} = \dot{m} \bullet c_p \bullet (T_{in} - T_{out}) - S_{cap} - S_{loss} \tag{8}$$

with the mass flow and the heat capacity of the HTF $\dot{m}$ and c_p. The inlet and the outlet temperature of the HTF are T_{in} and T_{out}, respectively. The enthalpy of the HTF, the capsule wall and the storage container, etc., are combined in H^* and the heat transfer to the PCM is included via the source term S_{cap}. Finally, heat losses are accounted for with the source term S_{loss}. Eq. (8) was discretized and solved with an explicit Euler scheme for the enthalpy at the new time level H^*. Here, T_{out} is set to the HTF temperature of the old time step T_{HTF}^{old}, which is determined from H^{*old}. The value of S_{cap} (corresponding to $\dot{Q}$ in Fig. 1) is read from a look-up table generated from CFD results. The discretization of the look-up table is described in Section 3.3 and linear interpolation is used for values between the discretization steps. The input values of the look-up table are T_{HTF}^{old} and H_{cap}^{old} and – depending on the heat transfer correlation – also $\dot{m}$. The change of H_{cap} is described with Eq. (9)

$$\frac{\partial H_{cap}}{\partial t} = S_{cap} \tag{9}$$

and the source term S_{loss} in Eq. (8) is defined by Eq. (10)

$$S_{loss} = \frac{1}{R_{loss}} \bullet \left(T_{HTF}^{old} - T_{amb}\right) \bullet \frac{1}{n_{cells}}. \tag{10}$$

For the inlet and outlet cells, S_{cap} vanishes and H^* does not include the enthalpy of the capsule walls. The procedure of the algorithm for cells with a capsule is as follows:

- Calculate S_{loss} with Eq. (10) with values of the old time step
- Determine S_{cap} using the LUT with values of the old time step
- Calculate $\frac{\partial H^*}{\partial t}$ with the help of Eq. (8)
- Determine $\frac{\partial H_{cap}}{\partial t}$ with the help of Eq. (9)
- Update H_{cap}, H^* and T_{HTF} from H^*
- Continue to the next time step.

3.2.2. sys-CFD-PCM-air-wall

This model is similar to the *sys-CFD-PCM* model, but the results in the look-up table and H_{cap} also account for the capsule wall and the air. In consequence, H^* no longer includes the enthalpy of the capsule wall, and instead includes only the enthalpy of the HTF and the storage container, etc. The inlet and outlet cells are implemented identically to the *sys-CFD-PCM* model. The procedure of the algorithm is also identical.

3.2.3. sys-CFD-PCM-air-wall-HTF

In this model, the energy equation for cells with PCM capsules is different from the other two reduced-order models (see Eq. (11)).

$$\dot{m} \bullet c_p \bullet (T_{in} - T_{out}) - S_{cap} - S_{loss} = 0 \tag{11}$$

Eq. (11) is solved for T_{out}, while S_{cap} and S_{loss} are determined as before. The enthalpy of the HTF is now included in H_{cap}, while Eq. (9) is still used to calculate the change of H_{cap}. For the last and the first cells, the calculation procedure remains the same as for the other two reduced-order models, but the enthalpy of the storage container, etc., is allocated solely to the first and the last cells. The procedure of the algorithm is identical to the first two models except for the updating of T_{HTF}, which is here calculated based on an energy balance in the cell.

3.3. Parameter variation for the CFD models

For the CFD simulations, the boundary conditions listed in Table 3 were applied to perform a parameter variation. For each of these simulations, the thermal power dependent on the total energy (of the PCM for the *CFD-PCM* model, of the whole capsule for the *CFD-PCM-air-wall* model, and of the whole capsule plus the HTF pro rata for the *CFD-PCM-air-wall-HTF* model) is written into a look-up table. This leads to one look-up table per model giving the power dependent on the total energy and the HTF temperature and the mass flow or the heat transfer coefficient (the dependency on the heat transfer coefficient vanishes for the models with a fixed heat transfer coefficient). The wall has almost no influence on k, resulting in fairly identical supporting points for the *CFD-PCM* and the *CFD-PCM-air-wall* models.

3.4. Calculation of the deviation

Within this work, several deviations ϵ are calculated referring to T_{out}, $\dot{Q}$ and Q. The absolute mean deviation of the outlet temperature of the HTF is calculated with Eq. (12).

$$\epsilon_T = \frac{1}{t} \sum_{i=1}^{n_t} \left|T_{out} - T_{out,ref}\right|_i \bullet \Delta t. \tag{12}$$

Eqs. (13) and (14) determine the relative deviation concerning $\dot{Q}$ and Q, respectively:

$$\epsilon_{\dot{Q}}^{rel} = \frac{1}{t} \sum_{i=1}^{n_t} \frac{\left|\dot{Q} - \dot{Q}_{ref}\right|_i \bullet \Delta t}{\left|\dot{Q}_{ref}\right|_i} \tag{13}$$

$$\epsilon_{Q}^{rel} = \frac{1}{t} \sum_{i=1}^{n_t} \frac{\left|Q - Q_{ref}\right|_i \bullet \Delta t}{\left|Q_{ref}\right|_i} \tag{14}$$

The definitions of the reference values $T_{out,ref}$, $\dot{Q}_{ref}$ and Q_{ref} depend on the case under consideration. For checking the mesh independency of the CFD models, Q_{ref} refers to the results calculated with the finest mesh with 67,500 cells in the PCM domain. In the case of the independency study on the time step size of the reduced-order models, $\dot{Q}_{ref}$ refers to the smallest time step tested ($\Delta t = 0.1$ s). When comparing the results of the reduced-order models with the experimental results, the reference values are always those of the experiment.

4. Mesh independency study

The mesh independency was checked for the *CFD-PCM* models, while

Table 3
List of values for the parameter variation for the CFD models. For the CFD-PCM and the CFD-PCM-air-wall, the first three values for k correspond to the correlation for a plane wall (correlation "var") and the last value corresponds to a correlation of a concentric annular gap (correlation "fix") [33].

Model	Variable	Values	Units
CFD-PCM	ϑ_∞	22.5; 25; 27.5; 30.0; 32.5; 35.0	°C
	k	114; 121; 128; 285	W/(m² K)
CFD-PCM-air-wall	ϑ_∞	22.5; 25; 27.5; 30.0; 32.5; 35.0	°C
	k	114; 121; 128; 287	W/(m²K)
CFD-PCM-air-wall-HTF	ϑ_{in}	22.5; 25; 27.5; 30.0; 32.5; 35.0	°C
	$\dot{m}$	5.893; 6.565; 7.237	kg/*min*

the dependency on the time step was investigated for the reduced-order models. In Fig. 13, the results of the mesh independency study for the CFD model are presented. For all meshes tested, ϵ_Q^{rel} (with respect to the finest mesh tested) is about $1.2{\cdot}10^{-4}$–$2.2{\cdot}10^{-4}$, indicating that the results are already mesh-independent for 30,000 cells. Since only one CFD model was tested for one parameter combination ($\vartheta_\infty = 35°C$, $k = 285 W/(m^2\,K)$), a mesh of 60,000 cells in the PCM domain was used for all other simulations so as to have some buffer.

The influence of Δt on $\epsilon_{\dot{Q}}^{rel}$ (concerning the smallest Δt tested) of the *sys-CFD-PCM-air-wall-HTF* model is shown in Fig. 14 for *experiment 2*. A Δt of 1 s gives a satisfactory deviation to the smallest Δt of 0.1 s of about 1.2 %. Therefore, a Δt of 1 s is chosen for all further system simulations.

5. Results

The results of the reduced-order models are compared to three experiments with almost identical boundary and initial conditions (*experiment 1*, *experiment 2* and *experiment 3*). In Fig. 4, ϑ_{in} and ϑ_{out} for *experiment 1* and all system simulation models are plotted over time. Except for the beginning, the difference between ϑ_{in} and ϑ_{out} is small, even less than 1 K for large parts of the experiment. Apart from some deviations directly after the initial peak, the numerical results follow the experimental ones to a large extent. After 3000 s the *sys-CFD-PCM-air-wall-HTF* and the *sys-CFD-PCM-air-wall-fix* models show almost no difference from the experimental results. The results regarding the other two experiments (shown in Appendix A in Figs. 15 and 18) demonstrate the same behavior.

Fig. 5 presents $\dot{Q}$ over time for *experiment 1*, while the results regarding the other two experiments can be seen in Appendix A in Figs. 16 and 19. The results confirm those of the outlet temperature. Following a peak in $\dot{Q}$ of up to 7 kW, $\dot{Q}$ drops below 10 % of the peak power at about 2000 s. The deviations between the numerical and experimental results are similar to those of ϑ_{out}. Following some deviations after the $\dot{Q}$ peak, the numerical results – especially the results of the *sys-CFD-PCM-air-wall-HTF* and the *sys-CFD-PCM-air-wall-fix* models – follow the experimental ones.

A clearer view of the performance of the models can be achieved by comparing the transferred heat Q over time (Fig. 6). The deviation of the numerical results from the experimental ones regarding the final Q is, on average for all models and experiments, only 2.3 % with a maximum of 4.7 %; however, the slope of Q can differ significantly from the experimental results for certain models. The reduced-order models *sys-CFD-PCM-air-wall-HTF* and *sys-CFD-PCM-air-wall-fix* give results close to the experimental ones for all three experiments (see Fig. 5, as well as Figs. 17 and 20 in Appendix A); while all the other reduced-order models lead to significant differences in the Q slope. The experimental results do not differ noticeably among the different experiments and the largest deviations to the experimental results are present for the *sys-CFD-PCM-var* model.

The relative mean deviation of Q, called ϵ_Q^{rel}, is shown in Fig. 7 for all reduced-order models and experiments. The smallest ϵ_Q^{rel} can be seen for the *sys-CFD-PCM-air-wall-HTF* and the *sys-CFD-PCM-air-wall-fix* models, with 3.4–5.2 %, followed by the *sys-CFD-PCM-air-wall-var* and the *sys-CFD-PCM-fix* models with 8.4–9.9 %. The largest ϵ_Q^{rel} occurs for the *sys-CFD-PCM-var* model, with 14.9–15.5 %. Again, the results plotted for the temperature and the power confirm these results (see Fig. 8 for ϵ_T and Fig. 9 for $\epsilon_{\dot{Q}}^{rel}$). Interestingly, $\epsilon_{\dot{Q}}^{rel}$ is distinctively larger than ϵ_Q^{rel} for all cases. One of the reasons for this behavior is the fluctuations present with $\dot{Q}$ – even if the peaks are only shifted slightly, rather large deviations can occur.

Finally, the influence of the capsule wall material and thickness and how this is reflected by the *CFD-PCM* and the *CFD-PCM-air-wall* models is investigated. The *CFD-PCM-air-wall-HTF* model was not included in this study since, as shown above, the *CFD-PCM-air-wall* model with the "right" convective boundary condition mimics the results of the *CFD-PCM-air-wall-HTF* model to a very high degree. Only one CFD simulation ($\vartheta_\infty = 35°C$ and the fixed convective boundary condition) was done with each CFD model involved and no system simulations were performed, as the effect under study can already be seen solely with the CFD models and, consequently, much fewer simulations are necessary when following this approach. Applying this variation to the *CFD-PCM* model results in a simple adjustment of k, which is the reciprocal of the series resistance from convection and conduction through the capsule wall. Only the latter is affected by the variation and was adjusted depending on the capsule wall material and thickness. An aluminum capsule wall of 1 mm thickness gives the same rounded k as the 3 mm capsule wall and therefore identical results. In Fig. 10, the liquid fraction α is plotted over time for the different capsule wall configurations for the *CFD-PCM* model. Changing the capsule wall material to HDPE gives the expected result and slows down the melting process significantly, leading to an increase of 53 % in the melting time for the configuration with a 3 mm thick HDPE capsule wall compared to the configurations with an

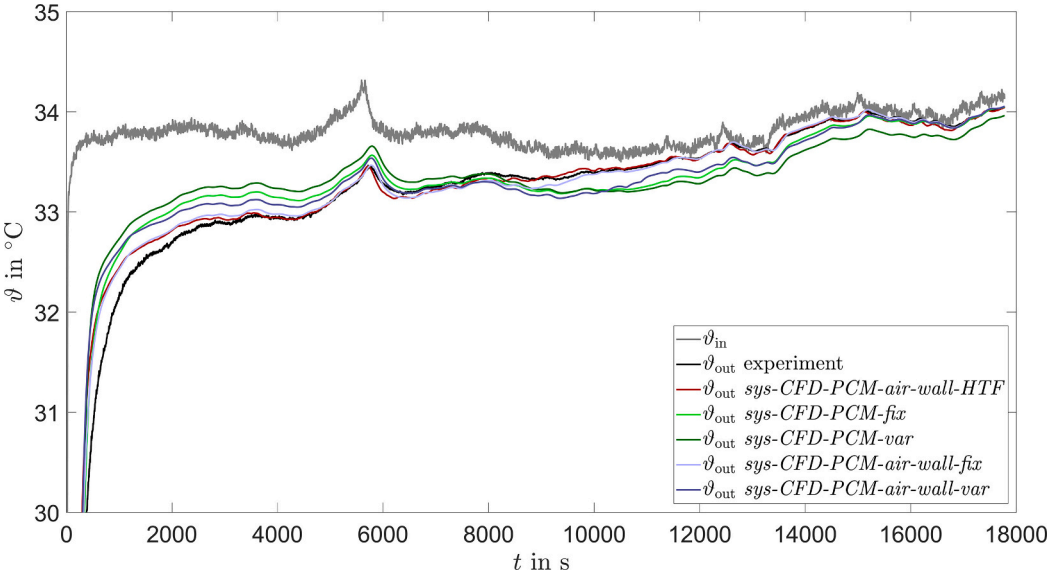

Fig. 4. Inlet temperature and experimental and numerical outlet temperatures of the HTF for experiment 1 plotted over time (zoomed to 30–35 °C).

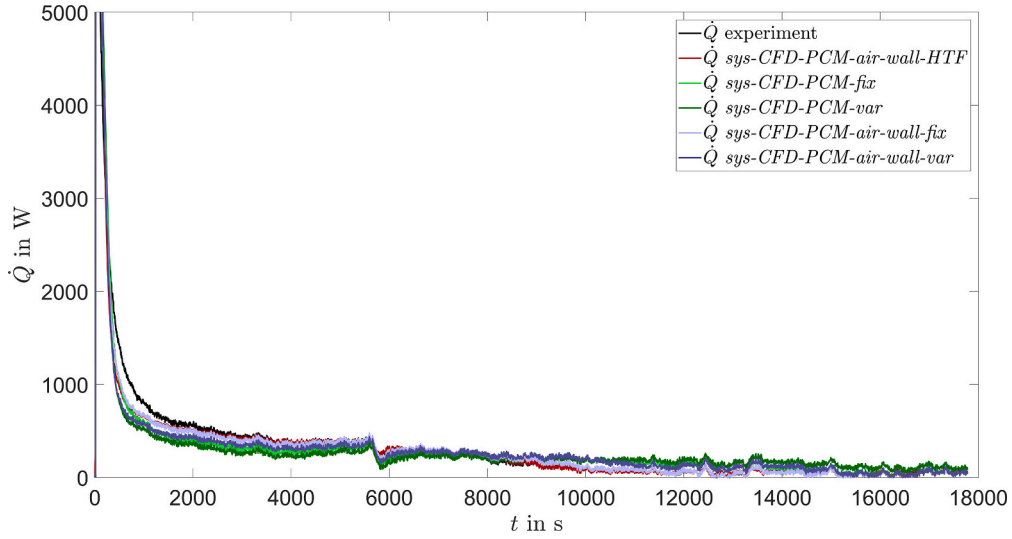

Fig. 5. Experimental and numerical $\dot{Q}$ over time for experiment 1 (zoomed to 0–5000 W).

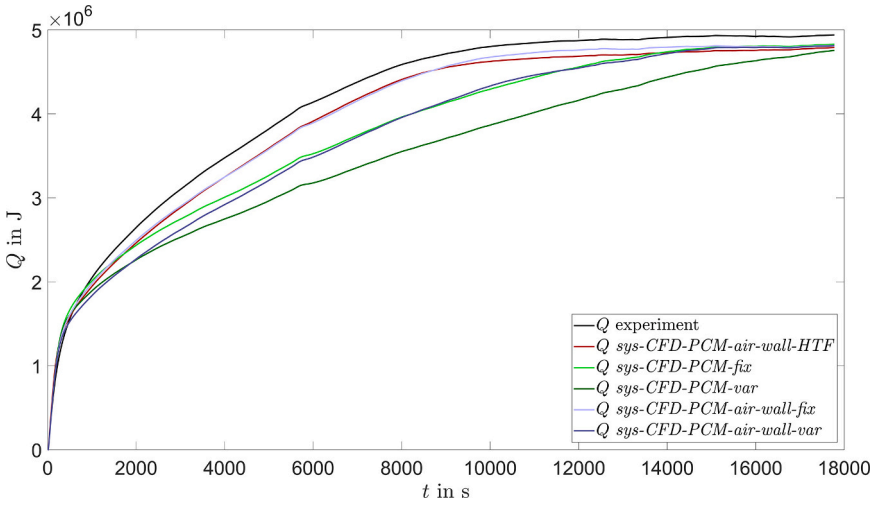

Fig. 6. Experimental and numerical Q over time for experiment 1.

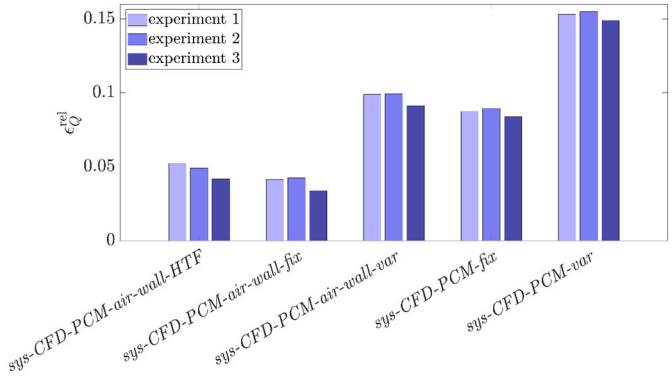

Fig. 7. The deviation ϵ_Q plotted for all three experiments and reduced-order models.

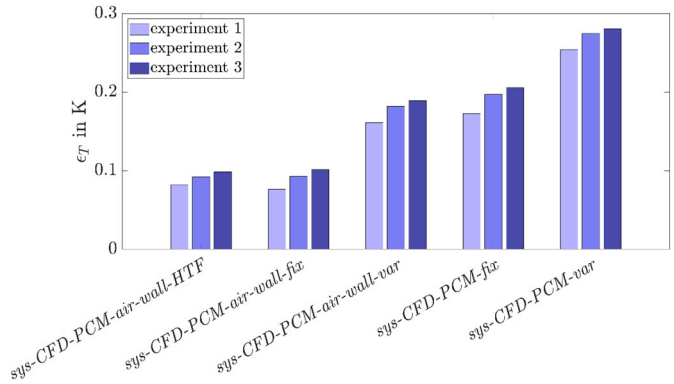

Fig. 8. The deviation ϵ_T plotted for all three experiments and reduced-order models.

aluminum capsule wall. For a 1 mm thick HDPE capsule wall, the increase in the melting time is 20 %.

When the capsule wall is included in the CFD model (*CFD-PCM-air-wall*), the results are very different (see Fig. 11). Still, the 3 mm thick aluminum capsule wall leads to the fastest melting, but the melting time is already distinctively higher (25 %) for the aluminum 1 mm capsule wall. Using HDPE as capsule material leads to much longer melting times, an increase of more than 140 % for 1 mm thickness and more than

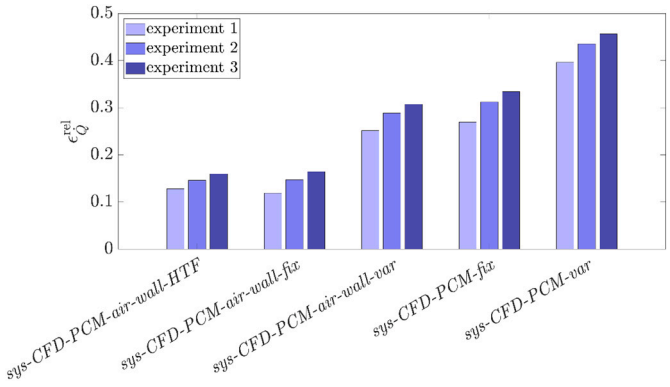

Fig. 9. The deviation $\epsilon_{\dot{Q}}$ plotted for all three experiments and reduced-order models.

150 % for 3 mm thickness. Interestingly, a thicker capsule wall leads to faster melting for the aluminum capsules; while, for the HDPE capsules, the melting is slowed down for thicker capsule walls.

Regarding the simulation times, the CFD models ranged from a few hours, for cases not including melting, up to more than two weeks for some cases involving melting. The very long simulation time resulted from the complexity of the model and the thin cells in the melt gap leading to small time step sizes – the average time step size for a simulation can drop to 0.05 s. The system simulations needed 20–60 s for the calculation itself (excluding setting up the simulation and reading data from external sources) with a very basic implementation. It was found that more than 90 % of the simulation time was spent reading from the look-up tables involving the *interp* functions from MATLAB, which are known to be slow. For one case tested, compiling the MATLAB code of the calculation to a C code mex-function already speeded up the simulation time from 22 s to 5 s. Compared to the CFD simulation this is about $8 \bullet 10^4$ times faster.

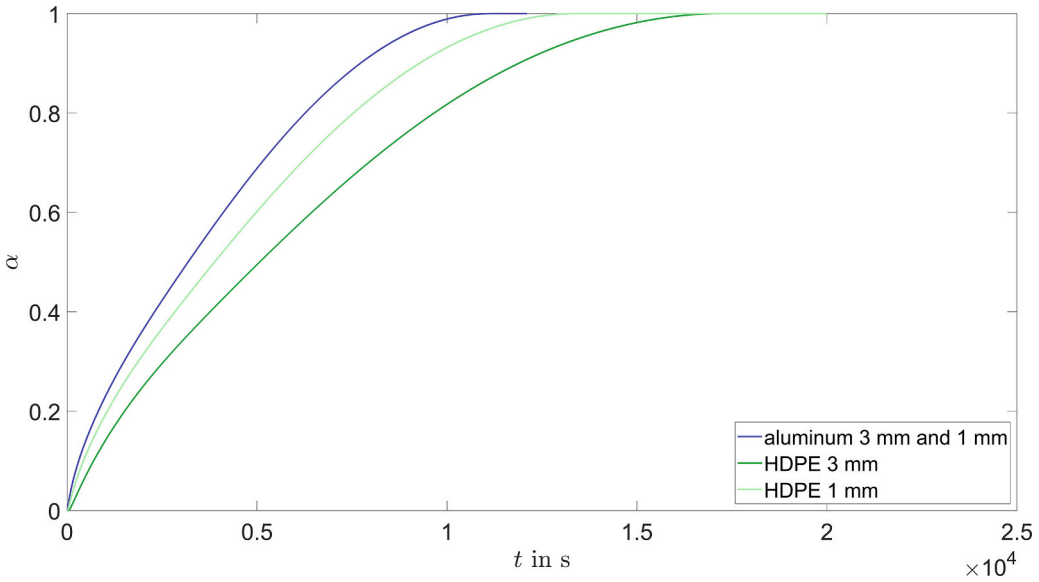

Fig. 10. The liquid fraction α plotted over time for different capsule walls and simulated with the CFD-PCM model ($\vartheta_\infty = 35°\mathrm{C}, k = 285\mathrm{W}/(\mathrm{m}^2\,\mathrm{K})$).

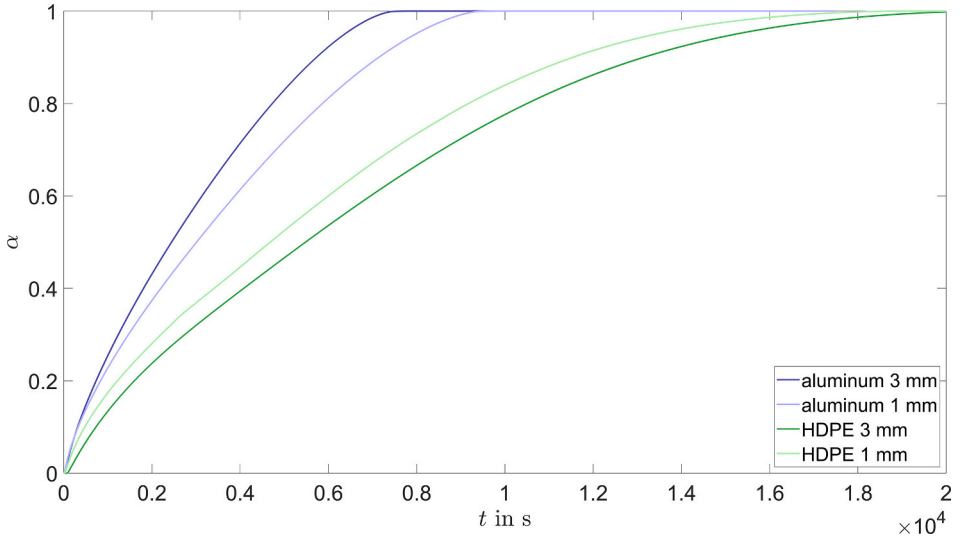

Fig. 11. The liquid fraction α plotted over time for different capsule walls simulated with the CFD-PCM-air-wall model ($\vartheta_\infty = 35°\mathrm{C}, k = 287\mathrm{W}/(\mathrm{m}^2\,\mathrm{K})$).

6. Discussion and conclusion

With the described approach of using results from detailed CFD simulations in reduced-order models for system simulation, satisfactory results can be achieved if the CFD simulation is performed properly. This directly leads to the first question raised in the introduction: "*Does the capsule wall and the HTF have to be included in the CFD model or can they be substituted by appropriate boundary conditions?*" As only the *sys-CFD-PCM-air-wall-HTF* and the *sys-CFD-PCM-air-wall-fix* models agree with the experimental results, it can be concluded that the capsule wall needs to be accounted for in the CFD model, but the HTF can be replaced by a properly defined boundary condition. However, defining the heat transfer coefficient with the help of correlations from the literature can be difficult in many cases and CFD simulations might be necessary to define the heat transfer coefficient between the HTF and the capsule wall. If the capsule wall is neglected in the CFD model and replaced by a heat transfer coefficient, distinctive deviations to the experimental results occur.

Moreover, there can even be misleading results when the effect of different capsule materials and wall thicknesses are studied with a model that has replaced the capsule wall by a heat transfer coefficient. The reason is that neglecting the capsule wall does not allow the heat flow through the capsule wall towards the bottom of the capsule to be taken into account. This heat flow is of great importance when close contact melting takes place as it enhances it drastically. That is why a thicker aluminum capsule wall leads to faster melting than a thin wall for the *sys-CFD-PCM-air-wall-fix* model; while the melting time does not change between the thick and the thin wall for the *sys-CFD-PCM-fix* model. On the contrary, a thicker HDPE capsule wall slows down the melting for both models. The reason is that, due to the low thermal conductivity of HDPE, almost no heat can flow from the side walls to the bottom of the capsule and therefore close contact melting plays only a minor role. For the setup studied, the main influence on the melting within the HDPE capsule was natural convection induced by heat transferred through the shell surface and this heat transfer rate decreases for thicker capsule walls.

Hummel et al. [18] showed that, during CCM of a PCM in a spherical macro-capsule, the temperature distribution on the capsule wall is transient and highly non-uniform and, therefore, the assumption commonly found in the literature of constant and uniform wall temperatures leads to significant errors for the investigated scenario. In general, we can confirm this statement for CCM in standing cylindrical capsules and add the following statements described above for our case: i) the capsule wall has to be included in the CFD model; and ii) the HTF might be replaced by a proper convective boundary condition.

The other questions listed in the introduction: "What is the accuracy of the simplified model?" and "How does the uncertainty compare to uncertainties reported in the literature for CFD simulations of LHTESSs?" will be addressed next. The deviation ϵ_Q^{rel} is about 5 % for the *sys-CFD-PCM-air-wall-HTF* and the *sys-CFD-PCM-air-wall-fix* models. This is surprisingly low, as we know from a basic uncertainty study on the melting process of a shell-and-tube LHTESS that, for instance, varying only one material property by 10 % can already lead to a variation in the energy content or the mean power in the same order of magnitude [34]. Furthermore, Beust et al. [22] reported an ϵ_Q^{rel} of 4–14 % for the simulation of a shell-and-tube LHTESS for a similar approach to the one presented here, but with a more complex simplified model. In addition, during the validation of the CCM solver used in this work, deviations to the experiments of about 11 % were seen on average for the melting time [15]. Even though, in the present study, the material properties were selected and processed very accurately [27] and the experiments were carried out with much diligence, we believe the deviations of only 5 % are too optimistic and some errors might have partially canceled each other out.

Regarding the simulation times, the following can be stated. Compared to the speed up from CFD to system simulation models reported in the literature (10–40 times [22] and 10–90 times [23]) the speed up for the present case is very high, with up to $8 \bullet 10^4$ times. This can lead to simulation times for the reduced-order models as low as 5 s. However, two aspects have to be considered here. First, the simulated LHTESS only had two layers and each additional layer would increase the simulation time most likely proportionally. Secondly, the large speed-up comes at a cost. For each model and heat transfer correlation combination, between 6 and 18 CFD simulations were performed. Each simulation lasted up to more than two weeks on one core of an Intel(R) Xeon(R) Gold 6252 CPU @ 2.10GHz computer. Therefore, this approach so far only makes sense if a large part of the CFD simulations can be run simultaneously on a workstation or cluster. This point might become even more severe for other applications, since in the present case the boundary conditions did not have large fluctuations, which allowed us to use only a few supporting points. For other applications, this might change with many more supporting points becoming necessary and, in consequence, more CFD simulations might be needed.

Nonetheless, the presented approach is very promising as long as a workstation or cluster is at hand to perform the CFD simulations simultaneously. In the future, the approach will be tested for more fluctuating boundary conditions, larger LHTESSs and different capsule geometries. Already, the approach will help to design LHTESSs with macro-encapsulated PCM in a fast and accurate manner.

Nomenclature

Variables and abbreviations

$\vec{a}$	Acceleration vector in $\mathrm{m/s^2}$
$\vec{A}$	Darcy term in $\mathrm{m/s^2}$
c_p	Specific heat capacity in $\mathrm{J/(kg \bullet K)}$
CCM	Close contact melting
CFD	Computational fluid dynamics
D	Darcy constant in $\mathrm{kg/(m^3 \bullet s)}$
$\vec{D}$	Viscous force in N
$\vec{F}$	Force vector in N
$\vec{g}$	Gravitational acceleration in $\mathrm{m/s^2}$
$\vec{G}$	Weight force in N
h	Specific enthalpy in J/kg
H	Enthalpy in J
H^*	Combined enthalpy in J
HTF	Heat transfer fluid
i	Count variable
I	Inertia term in N
k	Heat transfer coefficient in $\mathrm{W/(m^2 \bullet K)}$
LHTESS	Latent heat thermal energy storage system
LUT	Look-up table
m	Mass in kg
$\dot{m}$	Mass flow in kg/s
n	Count variable
p	Pressure in Pa
$\vec{P}$	Pressure force in N
PCM	Phase change material
Q	Heat in J
$\dot{Q}$	Heat flow in W
R	Thermal resistance in K/W
s	Surface in $\mathrm{m^2}$
S	Source term in W
t	Time in s
T	Temperature in K
$\vec{u}$	Velocity vector in m/s
V	Volume in $\mathrm{m^3}$

α	Liquid fraction
β	Volume expansion coefficient in $1/K$
ϵ	Deviation
ϵ	Small constant
ϑ	Temperature in $^\circ C$
λ	Thermal conductivity in $W/(m \bullet K)$
ν	Kinematic viscosity in m^2/s
ρ	Density in kg/m^3
τ	Viscous stress tensor in Pa

Subscripts

amb	Ambient
cap	Capsule
cells	Cells
HTF	Heat transfer unit
i	Count variable
in	Inlet
l	Liquid, liquidus
loss	Loss
out	Losses
Q	Heat
$\dot{Q}$	Heat flow
ref	Reference
s	Solid, solidus
set	Settling
t	Time step
T	Temperature
∞	Boundary condition

Superscripts

old	Old time step
rel	Relative

CRediT authorship contribution statement

Andreas König-Haagen: Conceptualization, Methodology, Software, Validation, Investigation, Resources, Data curation, Writing - Original draft preparation, Writing - Review & editing, Visualization.
Moritz Faden: Methodology, Software, Validation, Resources, Writing - Original draft preparation, Writing - Review & editing.
Gonzalo Diarce: Conceptualization, Validation, Resources, Writing - Review & editing.

Declaration of competing interest

The authors declare that they have no known competing financial interests or personal relationships that could have appeared to influence the work reported in this paper.

Data availability

Data will be made available on request.

Acknowledgments

Andreas König-Haagen is grateful for the financial support of the Deutsche Forschungsgemeinschaft (DFG, German Research Foundation) under Grant no KO 6286/1-1/444616738.

Moritz Faden is grateful for the financial support of the Deutsche Forschungsgemeinschaft (DFG, German Research Foundation) under grant no. BR 1713/20-2.

This work was partially funded by the ENEDI Research Group (IT1730-22) and by the Spanish Ministry of Science and Innovation (MICINN) through the STES4D research project (TED2021-131061B-C32).

Appendix A

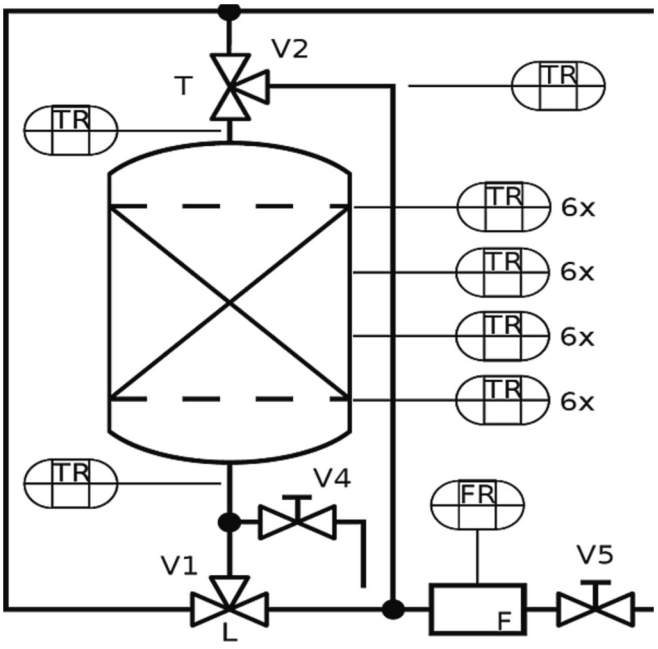

Fig. 12. Flow chart of the LHTESS.

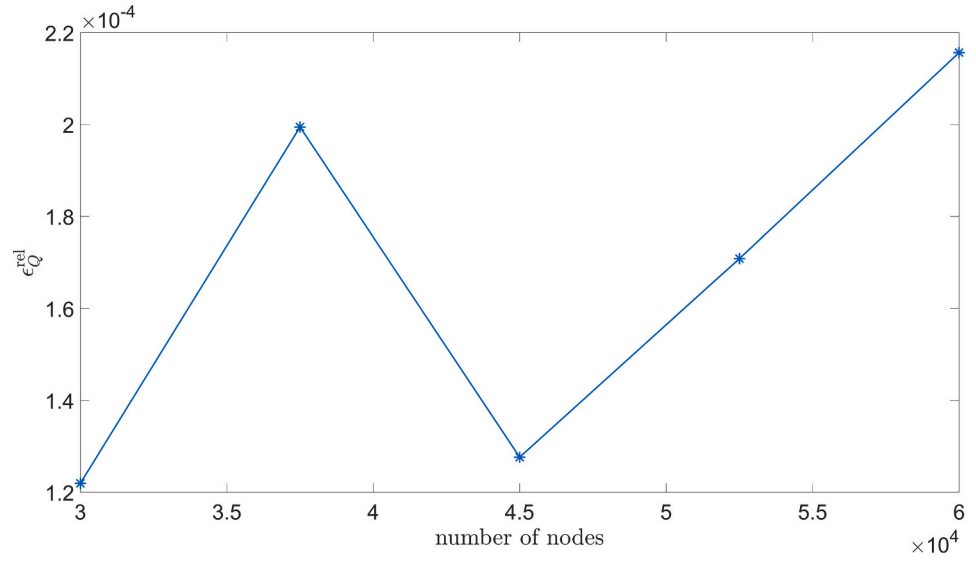

Fig. 13. For the CFD-PCM model ϵ_Q^{rel} is plotted for different meshes with respect to the finest mesh with 67,500 nodes.

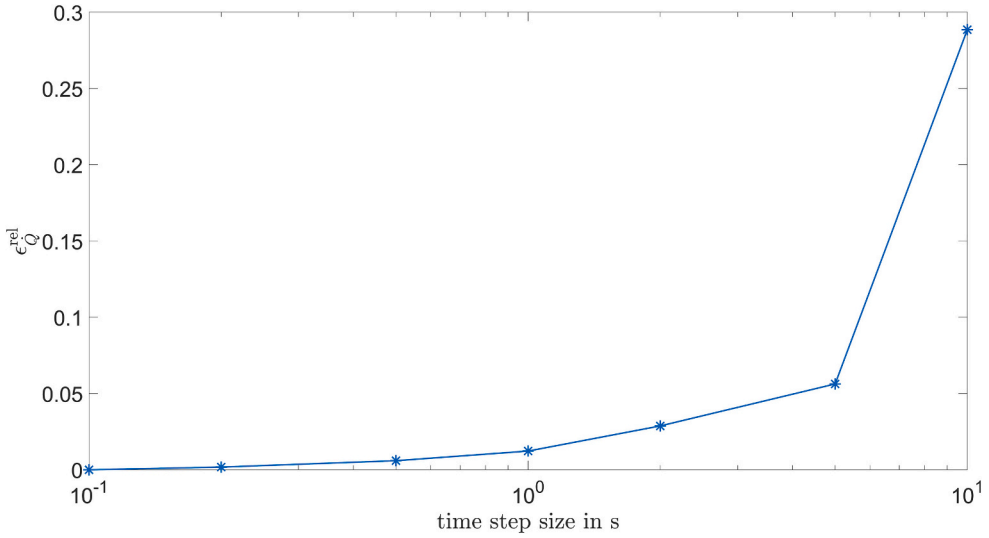

Fig. 14. For the sys-CFD-PCM-air-wall-HTF model $\epsilon_{\dot{Q}}^{rel}$ is plotted for different time step sizes with respect to the smallest time step size of 0.1 s.

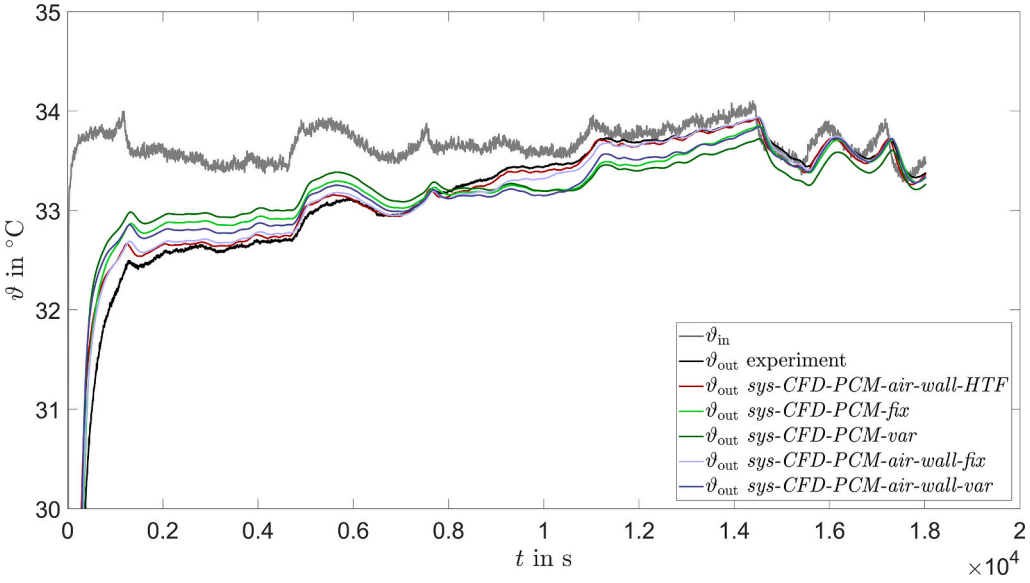

Fig. 15. Inlet temperature and experimental and numerical outlet temperatures of the HTF for experiment 2 plotted over time (zoomed to 30–35 °C).

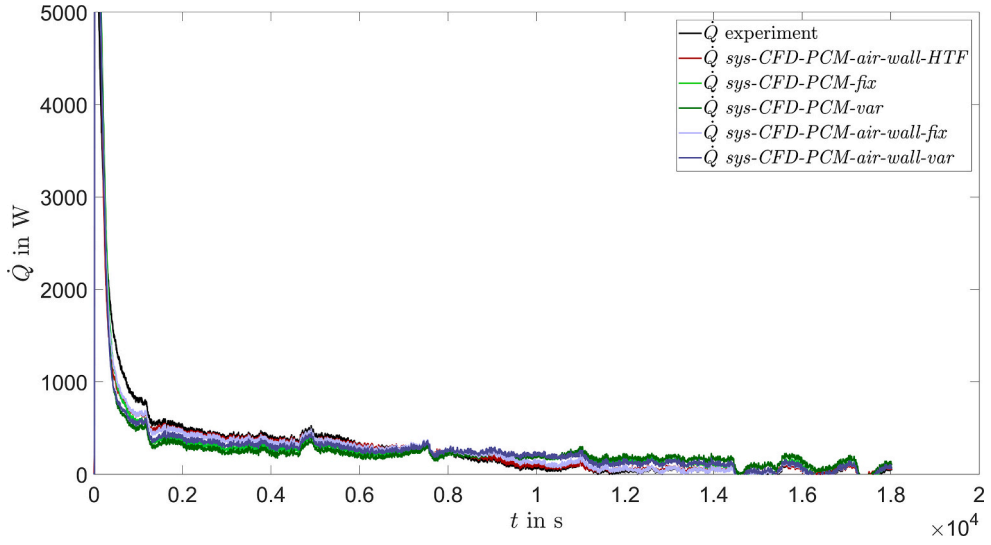

Fig. 16. Experimental and numerical $\dot{Q}$ over time for experiment 2 (zoomed to 0–5000 W).

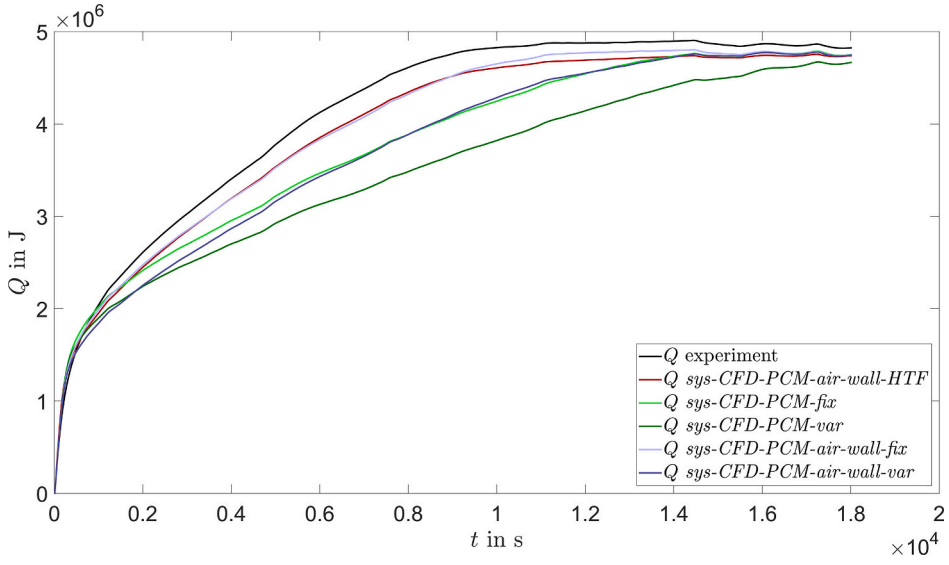

Fig. 17. Experimental and numerical Q over time for experiment 2.

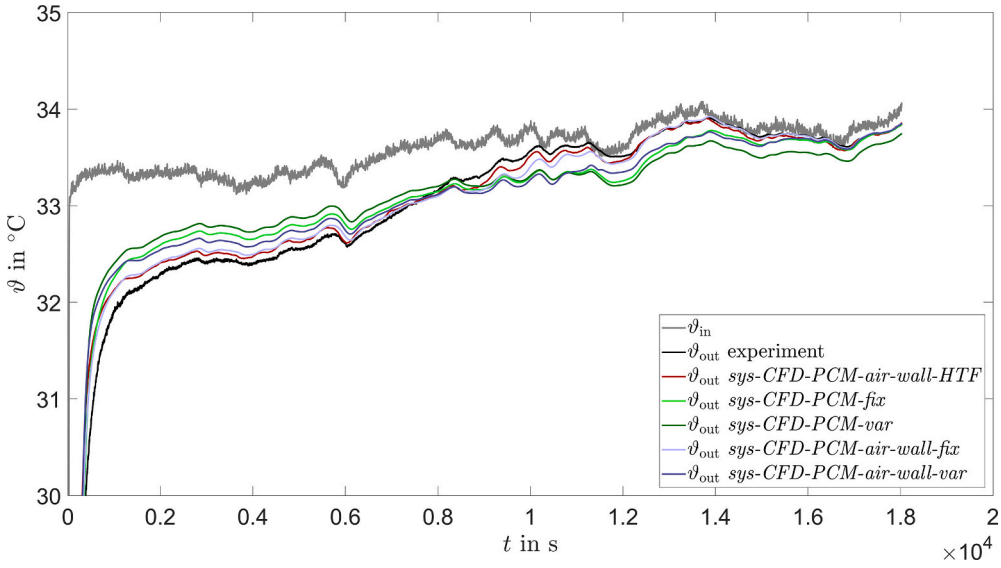

Fig. 18. Inlet temperature and experimental and numerical outlet temperatures of the HTF for experiment 3 plotted over time (zoomed to 30–35°C).

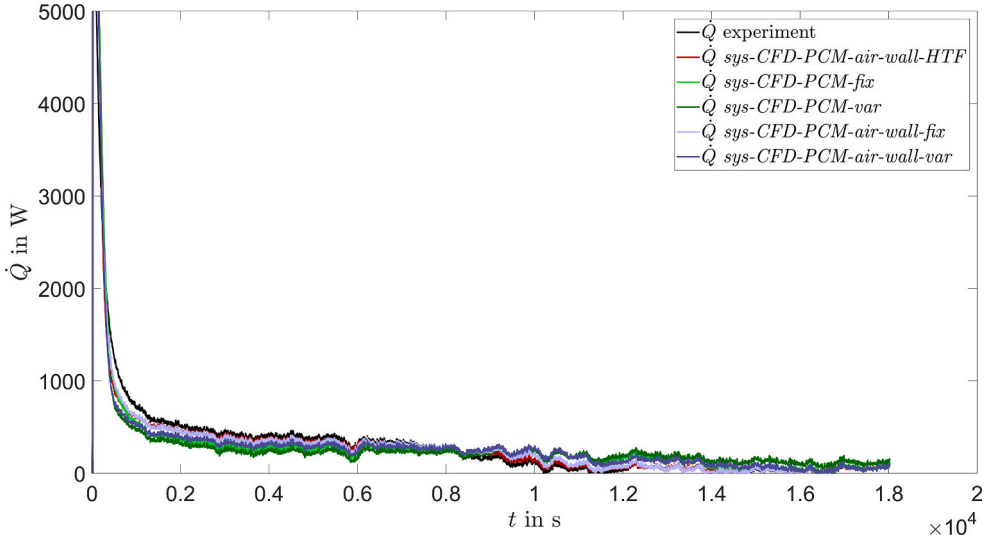

Fig. 19. Experimental and numerical $\dot{Q}$ over time for experiment 3 (zoomed to 0–5000 W).

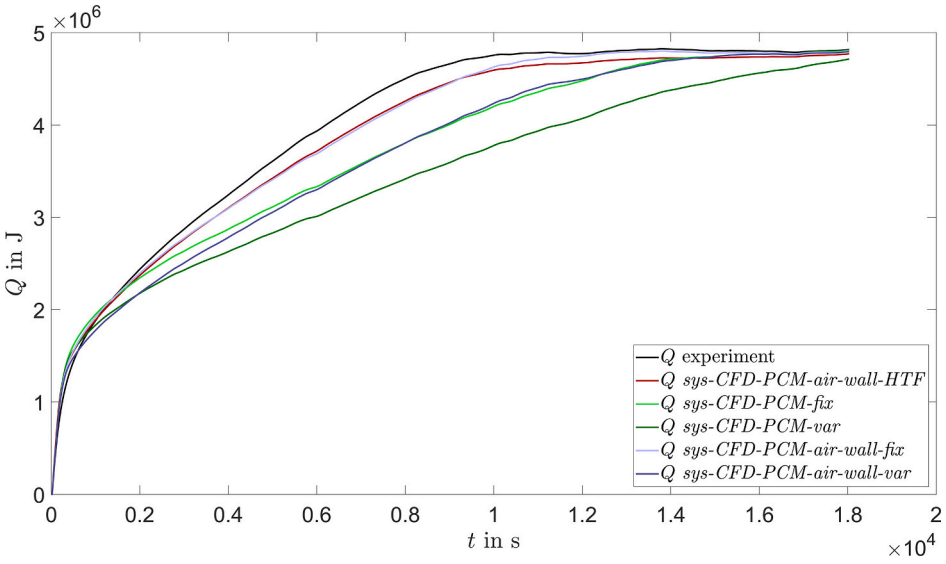

Fig. 20. Experimental and numerical Q over time for experiment 3.

References

[1] H. Mehling, L.F. Cabeza, Heat and Cold Storage With PCM: An Up To Date Introduction Into Basics and Applications, Springer-Verlag, Berlin, Heidelberg, 2008, ISBN 978-3-540-68557-9.

[2] S. Höhlein, A. König-Haagen, D. Brüggemann, Macro-encapsulation of inorganic phase-change materials (PCM) in metal capsules, Materials 11 (2018) 1752, https://doi.org/10.3390/ma11091752.

[3] V.R. Voller, An overview of numerical methods for solving phase change problems, in: W.J. Minkowycz, E.M. Sparrow (Eds.), Advances in Numerical Heat Transfer, Taylor & Francis, New York, NY, 1997, pp. 341–380.

[4] V.R. Voller, C.R. Swaminathan, B.G. Thomas, Fixed grid techniques for phase change problems: a review, Int. J. Numer. Methods Eng. 30 (1990) 875–898.

[5] Y. Dutil, D.R. Rousse, N.B. Salah, S. Lassue, L. Zalewski, A review on phase-change materials: mathematical modeling and simulations, Renew. Sust. Energ. Rev. 15 (2011) 112–130, https://doi.org/10.1016/j.rser.2010.06.011.

[6] A.D. Brent, V.R. Voller, K.J. Reid, Enthalpy-porosity technique for modeling convection-diffusion phase change: application to the melting of a pure metal, Numer. Heat Transfer Part A Appl. 13 (1988) 297–318.

[7] C.R. Swaminathan, V.R. Voller, On the enthalpy method, Int. J. Numer. Methods Heat Fluid Flow 3 (1993) 233–244, https://doi.org/10.1108/eb017528.

[8] A. König-Haagen, G. Diarce, Comparison of corrected and uncorrected enthalpy methods for solving conduction-driven solid/liquid phase change problems, Energies 16 (2023) 449, https://doi.org/10.3390/en16010449.

[9] Y. Asako, M. Faghri, M. Charmchi, P.A. Bahrami, Numerical solution for melting of unfixed rectangular phase-change material under low-gravity environment, Numer. Heat Transfer Part A Appl. 25 (1994) 191–208, https://doi.org/10.1080/10407789408955944.

[10] B. Ghasemi, M. Molki, Melting of unfixed solids in square cavities, Int. J. Heat Fluid Flow 20 (1999) 446–452, https://doi.org/10.1016/S0142-727X(99)00025-9.

[11] R.R. Kasibhatla, A. König-Haagen, F. Rösler, D. Brüggemann, Numerical modelling of melting and settling of an encapsulated PCM using variable viscosity, Heat Mass Transf. (2016) 1–10, https://doi.org/10.1007/s00231-016-1932-0.

[12] K. Schüller, J. Kowalski, Spatially varying heat flux driven close-contact melting – a Lagrangian approach, Int. J. Heat Mass Transf. 115 (2017) 1276–1287, https://doi.org/10.1016/j.ijheatmasstransfer.2017.08.092.

[13] Y. Kozak, G. Ziskind, Novel enthalpy method for modeling of PCM melting accompanied by sinking of the solid phase, Int. J. Heat Mass Transf. 112 (2017) 568–586, https://doi.org/10.1016/j.ijheatmasstransfer.2017.04.088.

[14] N. Hu, Z.-R. Li, Z.-W. Xu, L.-W. Fan, Rapid charging for latent heat thermal energy storage: a state-of-the-art review of close-contact melting, Renew. Sust. Energ. Rev. 155 (2022), 111918, https://doi.org/10.1016/j.rser.2021.111918.

[15] M. Faden, A. König-Haagen, S. Höhlein, D. Brüggemann, An implicit algorithm for melting and settling of phase change material inside macrocapsules, Int. J. Heat Mass Transf. 117 (2018) 757–767, https://doi.org/10.1016/j.ijheatmasstransfer.2017.10.033.

[16] F. Rösler, Modellierung und Simulation der Phasenwechselvorgänge in makroverkapselten latenten thermischen Speichern, Logos Verlag Berlin GmbH, 2014.

[17] T. Shockner, G. Ziskind, Experimental and numerical evaluation of phase-change material performance in a vertical cylindrical capsule for thermal energy storage, Appl. Therm. Eng. 119519 (2022), https://doi.org/10.1016/j.applthermaleng.2022.119519.

[18] D. Hummel, S. Beer, A. Hornung, A conjugate heat transfer model for unconstrained melting of macroencapsulated phase change materials subjected to external convection, Int. J. Heat Mass Transf. 149 (2020), https://doi.org/10.1016/j.ijheatmasstransfer.2019.119205.

[19] R.R. Kasibhatla, D. Brüggemann, Coupled conjugate heat transfer model for melting of PCM in cylindrical capsules, Appl. Therm. Eng. 184 (2021), https://doi.org/10.1016/j.applthermaleng.2020.116301.

[20] F.A. Regin, S.C. Solanki, J.S. Saini, An analysis of a packed bed latent heat thermal energy storage system using PCM capsules: numerical investigation, Renew. Energy 34 (2009) 1765–1773, https://doi.org/10.1016/j.renene.2008.12.012.

[21] K.A. Ismail, J.R. Henriquez, Numerical and experimental study of spherical capsules packed bed latent heat storage system, Appl. Therm. Eng. 22 (2002) 1705–1716.

[22] C. Beust, E. Franquet, J.-P. Bédécarrats, P. Garcia, Predictive approach of heat transfer for the modelling of large-scale latent heat storages, Renew. Energy 157 (2020) 502–514, https://doi.org/10.1016/j.renene.2020.04.135.

[23] C. Beust, E. Franquet, J.-P. Bédécarrats, P. Garcia, J. Pouvreau, J.-F. Fourmigué, Multi-scale modelling of a large scale shell-and-tube latent heat storage system for direct steam generation power plants, in: SOLARPACES 2019: International Conference on Concentrating Solar Power and Chemical Energy Systems. SOLARPACES 2019: International Conference on Concentrating Solar Power and Chemical Energy Systems, Daegu, South Korea, 1–4 October 2019, AIP Publishing, 2020, p. 190002.

[24] R.R. Kasibhatla, Multiscale Thermo-fluid Modelling of Macro-encapsulated Latent Heat Thermal Energy Storage Systems, Logos Verlag, Berlin, 2019, ISBN 3832548939.

[25] A. König-Haagen, M. Faden, J. Gleißl, G. Diarce, D. Brüggemann, Development and analysis of a CFD results based system simulation model for a latent heat thermal energy storage unit with macro-capsules, in: 15th International Virtual Conference on Energy Storage (Enerstock 2021), 2021, p. 208.

[26] D. Brüggemann, A. König-Haagen, R.R. Kasibhatla, S. Höhlein, U. Glatzel, R. Völkl, N. Agarkov, Entwicklung makroverkapselter Latentwärmespeicher für den Transport von Abwärme (MALATrans). Abschlussbericht: Laufzeit: 01.07.2013 bis 31.12.2016, Bayreuth, 2017.

[27] M. Faden, S. Höhlein, J. Wanner, A. König-Haagen, D. Brüggemann, Review of thermophysical property data of octadecane for phase-change studies, Materials 12 (2019) 2974, https://doi.org/10.3390/ma12182974.

[28] H.G. Weller, G. Tabor, H. Jasak, C. Fureby, A tensorial approach to computational continuum mechanics using object-oriented techniques, Comput. Phys. 12 (1998) 620, https://doi.org/10.1063/1.168744.

[29] V.R. Voller, C. Prakash, A fixed grid numerical modelling methodology for convection-diffusion mushy region phase-change problems, Int. J. Heat Mass Transf. 30 (1987) 1709–1719, https://doi.org/10.1016/0017-9310(87)90317-6.

[30] V.R. Voller, C.R. Swaminathan, General source-based method for solidification phase change, Numer. Heat Transfer, Part B 19 (1991) 175–189, https://doi.org/10.1080/10407799108944962.

[31] M. Faden, A. König-Haagen, E. Franquet, D. Brüggemann, Influence of density change during melting inside a cavity: theoretical scaling laws and numerical analysis, Int. J. Heat Mass Transf. 173 (2021), 121260, https://doi.org/10.1016/j.ijheatmasstransfer.2021.121260.

[32] R.I. Issa, Solution of the implicitly discretised fluid flow equations by operator-splitting, J. Comput. Phys. 62 (1986) 40–65, https://doi.org/10.1016/0021-9991(86)90099-9.
[33] VDI, VDI-Wärmeatlas, 11., bearb. und erw. Aufl, Springer-Verlag, Berlin, Heidelberg, 2013.
[34] A. König-Haagen, A. Mühlbauer, T. Marquardt, A. Caron-Soupart, J.-F. Fourmigué, D. Brüggemann, Basic analysis of uncertainty sources in the CFD simulation of a shell-and-tube latent thermal energy storage unit, Appl. Sci. 10 (2020) 6723, https://doi.org/10.3390/app10196723.